Microscopy AND
Microanalysis

Calcium Deposits in the Crayfish, *Cherax quadricarinatus*: Microstructure Versus Elemental Distribution

Gilles Luquet,[1,*] Yannicke Dauphin,[2] Aline Percot,[3] Murielle Salomé,[4] Andreas Ziegler,[5] Maria S. Fernández,[6] and José L. Arias[6]

[1]*Sorbonne Universités, Biologie des Organismes et des Ecosystèmes Aquatiques (BOREA), UMR MNHN/CNRS-7208/UPMC/UCN/UA/IRD-207, Muséum National d'Histoire Naturelle, 75005 Paris, France*
[2]*Sorbonne Universités, Département Systèmatique et Evolution, Mammifères et Oiseaux, Muséum National d'Histoire Naturelle, 75005 Paris, France*
[3]*Sorbonne Universités, MONARIS, UMR 8233 CNRS/UPMC, Université Paris 06, 75005 Paris, France*
[4]*ID21, European Synchrotron Radiation Facility, 38000 Grenoble, France*
[5]*Central Facility for Electron Microscopy, University of Ulm, 89069 Ulm, Germany*
[6]*Faculty of Veterinary and Animal Sciences, University of Chile, Santiago de Chile, Chile*

Abstract: The crayfish *Cherax quadricarinatus* stores calcium ions, easily mobilizable after molting, for calcifying parts of the new exoskeleton. They are chiefly stored as amorphous calcium carbonate (ACC) during each premolt in a pair of gastroliths synthesized in the stomach wall. How calcium carbonate is stabilized in the amorphous state in such a biocomposite remains speculative. The knowledge of the microstructure at the nanometer level obtained by field emission scanning electron microscopy and atomic force microscopy combined with scanning electron microscopy energy-dispersive X-ray spectroscopy, micro-Raman and X-ray absorption near edge structure spectroscopy gave relevant information on the elaboration of such an ACC-stabilized biomineral. We observed nanogranules distributed along chitin-protein fibers and the aggregation of granules in thin layers. AFM confirmed the nanolevel structure, showing granules probably surrounded by an organic layer and also revealing a second level of aggregation as described for other crystalline biominerals. Raman analyses showed the presence of ACC, amorphous calcium phosphate, and calcite. Elemental analyses confirmed the presence of elements like Fe, Na, Mg, P, and S. P and S are heterogeneously distributed. P is present in both the mineral and organic phases of gastroliths. S seems present as sulfate (probably as sulfated sugars), sulfonate, sulfite, and sulfoxide groups and, in a lesser extent, as sulfur-containing amino acids.

Key words: amorphous calcium carbonate, amorphous calcium phosphate, biomineralization, calcium storage, organic matrix

INTRODUCTION

Crustaceans are able to synthesize and resorb calcified biominerals during molting cycles (Greenaway, 1985; Lowenstam & Weiner, 1989; Luquet & Marin, 2004; Luquet, 2012). Due to the presence of a hard and inelastic exoskeleton, they have to molt in order to grow. Among the arthropods, most crustaceans have the ability to harden their exoskeleton by sclerotization and calcification. This last process occurs by precipitation of calcium carbonate and, to a lesser extent, calcium phosphate as amorphous calcium phosphate (ACP) or carbonate apatite in a three-dimensional network of organic matter synthesized by hypodermal cells. This has been mainly studied in decapods (Soejoko & Tjia, 2003; Dillaman et al., 2005; Romano et al., 2007; Kunkel & Jercinovic, 2013; Grunenfelder et al., 2014) and isopods (Becker et al., 2005; Neues et al., 2007).

Calcium ions are more or less available in the aquatic biotopes and branchial calcium uptake constitutes the major cuticular contribution of calcium ions for aquatic species in postmolt. Nevertheless, for terrestrial and semiterrestrial species, premolt periods are devoted, among other processes, to the storage of calcium ions. Such a storage process was described in isopods, amphipods, and decapods (Graf, 1978; Greenaway, 1985; Luquet, 2012). In this last group, land crabs (Numanoi, 1939; Bliss, 1953) and aquatic decapods such as lobsters (Herrick, 1911), Norway lobsters (Farmer, 1973; Sarda, 1991), and crayfish (Kugler & Birkner, 1948; Travis, 1960, 1963; Chantran, 1874; Huxley, 1879) develop gastroliths in their cardiac stomach wall as reservoirs of mineral ions.

Gastroliths are structurally "rounded, disc-shaped" (Travis, 1960, 1963) and often semispherical (Fig. 1). They are synthesized in two specialized discoidal areas by epithelial cells between the stomach epithelium and a noncalcified cuticle underlying this epithelium (Travis, 1963; Shechter et al., 2008a; Glazer & Sagi, 2012). The mineral phase, which originates from decalcification of the old carapace, is
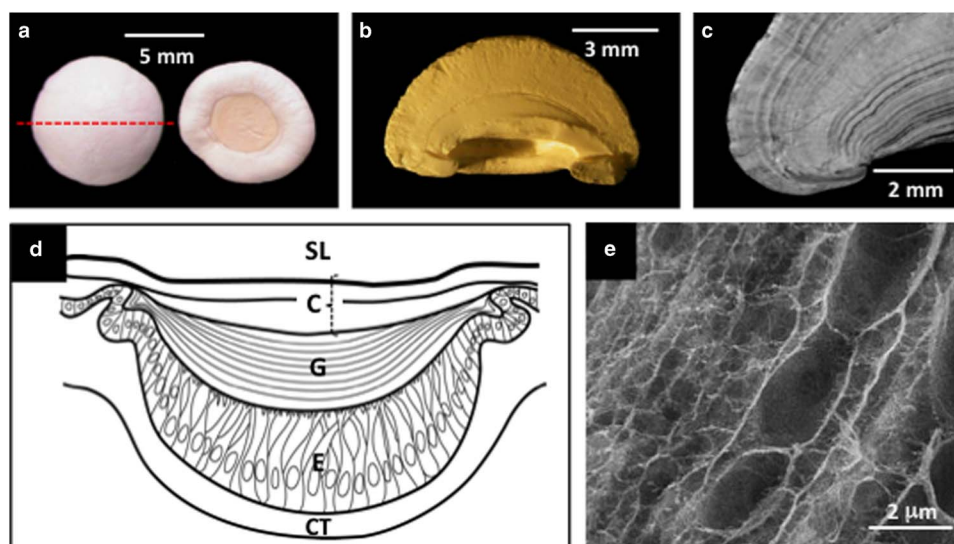
Figure 1. a: Pair of hemispherical gastroliths from the freshwater crayfish, *Cherax quadricarinatus*. At left: rounded side in contact with the stomach epithelium. At right: flat face on the cuticle side. The dashed line indicates where cross-sections were performed perpendicular to the surface. **b:** Natural fracture of a gastrolith showing the dense mineralized inner structure. **c:** Cross-section of a gastrolith showing the layered structure (**a–c:** light microscopy). **d:** Gastrolith disc section (modified from Travis, 1963). **e:** Gastrolith organic matrix composed of parallel and transverse chitin-protein fibers (after slight decalcification by acetic acid; SEM picture). SL = stomach lumen; C = cuticle comprised of epicuticle, exocuticule, and endocuticle, from top to bottom; G = gastrolith; E = stomach epithelium; Ct = connective tissue; SEM = scanning electron microscopy.

precipitated within an organic template of chitin-protein fibers tightly linked by protein bridges (Thormann et al., 2012; Luquet et al., 2013; see also Fig. 1). Different categories of molecules have been identified as organic components: proteins with putative posttranslational modifications (Ishii et al., 1996; Tsutsui et al., 1999; Shechter et al., 2008a, 2008b; Luquet et al., 2009; Bentov et al., 2010; Glazer et al., 2010, 2013; Glazer & Sagi, 2012), proteoglycans and carbohydrates (Fernandez et al., 2012; Luquet et al., 2013), and phosphorylated low-molecular weight metabolites (Bentov et al., 2010; Akiva-Tal et al., 2011; Sato et al., 2011).

These deposits are mainly composed of amorphous calcium carbonate, or ACC, the most metastable of the calcium carbonate polymorphs (Hikida et al., 2003; Shechter et al., 2008a; Luquet, 2012; Luquet et al., 2013). The presence of stable ACC in biocomposites has already been described, especially in crustaceans (Addadi et al., 2003; Luquet, 2012). Recently, another amorphous mineral, ACP, was suggested to also be present in gastroliths (Luquet et al., 2013; Reeder et al., 2013; Habraken et al., 2015).

Numerous hypotheses have been forwarded to explain biogenic ACC stabilization over time (Aizenberg et al., 2001). Mineral ions such as Mg^{2+} are suspected of playing such a role (Loste et al., 2003; Raz et al., 2003; Han & Aizenberg, 2008; Politi et al., 2008). Anion groups (carboxyl, sulfate, phosphate) from components of organic matrices (proteins without or with posttranslational modifications, carbohydrates, proteoglycans putatively sulfated) are known to chelate calcium ions and are considered to play a role in ACC formation/stabilization.

In gastroliths, compounds suspected of playing such a role are proteins with putative posttranslational modifications (Shechter et al., 2008b; Bentov et al., 2010; Glazer et al., 2010). On the other hand, small phosphorylated metabolites have also been detected by nuclear magnetic resonance (NMR) and are thought to play an interacting role between chitin-binding proteins or protein-binding proteins and calcium ions preventing a crystallization process (Akiva-Tal et al., 2011; Sato et al., 2011).

One strategy to find an answer is to explore the relationship occurring between the morphology/structure of the gastrolith, the mineral, the elemental and molecular composition, and the spatial distribution of all these components. Analyses previously undertaken were rarely performed *in situ* and most of the results were obtained from bulk extracts. Here we analyzed the structure of *Cherax quadricarinatus* gastroliths from the microscale to the nanometer level by using high-performance microscopy techniques such as field emission scanning electron microscopy (FESEM) and atomic force microscopy (AFM). In parallel, we investigated the presence and distribution of elements (P, S, Mg, Sr, Fe, …) on gastrolith cross-sections by scanning electron microscopy energy-dispersive X-ray spectroscopy (SEM-EDS) and Raman spectroscopy. This analysis reveals a particular spatial-temporal distribution of some elements (S and P more particularly). Finally, we investigated in more depth the presence and distribution of S by X-ray absorption near edge structure spectroscopy (XANES).

MATERIALS AND METHODS

Gastrolith Sample Preparation

Australian red claw crayfish, *C. quadricarinatus*, were bred in a farm located on the campus of the University of Chile, Santiago de Chile. Gastroliths were extracted from animals at ecdysis, the period of the molting cycle where gastroliths are at their maximum size. They were immersed in 10% (v/v) NaOCl for a few hours to remove superficial organic contaminants and then rinsed with distilled water and kept at room temperature and dry air until used.

Sections were obtained by cutting gastroliths with an electric microsaw. Sections were cut perpendicular to the surface (dashed line, Fig. 1a) symmetrically through the center of the flat circular basis of the semispherical gastrolith. Two types of sectioning were performed: cross-sections after embedding the gastroliths in araldite for obtaining slices of 50-μm thickness and sections of whole gastroliths in two halves without any previous treatment. In the latter case, some sections were polished as described for the different techniques.

For observing *in situ* the organic matrix network, freshly broken gastroliths were incubated in acetic acid 5% (30 s) to slightly decalcify the surface. Then, they were carefully rinsed with methanol and air-dried before observation.

The soluble organic matrix (SOM) was obtained after grinding gastroliths to a powder. This powder was decalcified for 24 h in cold acetic acid (10% v/v) at 4°C. The solution was then centrifuged 30 min at 4,000 g at 4°C. The supernatant containing the acetic acid-SOM was filtered and concentrated with an Amicon ultrafiltration system (Millipore SAS, Molsheim, France) on an Ultracel-PL membrane (5-kDa cut-off; Millipore SAS, Molsheim, France). The SOM solution, devoid of acetic acid, was lyophilized and kept at 4°C until used.

Light and FESEM Observations

For light microscopy observations, gastroliths were used after extraction and washing. The two types of transverse sections obtained as described above were observed using a Nikon Eclipse E200 microscope or a Nikon SMZ800 binocular stereomicroscope (Nikon France SAS, Champigny sur Marne, France).

For FESEM observations, gastroliths were cleaved in two halves and mounted on aluminum holders using self-adhesive carbon pads and conductive glue without any polishing. Samples were then rotary shadowed with 3.5–4 nm platinum at an angle of 45° using a BAF 300 (BAL-TEC, Balzers, Liechtenstein). FESEM (Hitachi S-5,200; Hitachi High-Tech Science Corporation, Tokyo, Japan) was performed at an acceleration voltage of 4 kV and an emission current of 10 μA.

AFM

Samples were also studied using a Nanoscope IIIa Dimension 3100 scanning probe microscope (Digital Instruments-Veeco, Santa Barbara, CA, USA) operated in tapping mode in air. The AFM tapping mode uses an oscillating tip at an amplitude of approximately several tens of nanometers when the tip is not in contact with the surface. Since the tip is no longer in permanent contact with the sample surface during the scanning motion, unwanted alterations can be avoided to a large extent. The resolution of tapping mode AFM is on the order of a few nanometers. Measurements with an AFM are made in three dimensions, the horizontal X-Y plane and the vertical Z dimension. Tip-sample force interactions cause changes in amplitude, phase, and the resonance frequency of the oscillating cantilever. The spatial variation of the change can be presented in height (topography) or interaction (amplitude or phase) images that can be collected simultaneously. Phase imaging is a powerful extension that provides nanometer-scale information about surface structure: it monitors the phase lag between the signal that drives the cantilever to oscillate and the cantilever oscillation output signal. Thus, contrast in phase images is due to differences in material properties. The phase lag is monitored while the topographic image is being taken so that images of topography and material properties are collected simultaneously. The amplitude AFM signal is related to the gradient of the topography as the tip scans over the sample surface. Fine morphological features are easily observed in amplitude and phase images.

Compared with SEM, AFM provides topographic direct height measurements and views of surface features since no coating is necessary. Compared with TEM, three-dimensional AFM images are obtained without difficult sample preparation and with a similar resolution.

Sample sections were polished using P1,200, P2,500, and P4,000 HERMES water grinding papers (Buehler, Dardilly, France), 3 and 1 μm diamond polycrystalline suspensions (Buehler, Dardilly, France). To avoid analytical artifacts, no aluminum oxide suspension was used because previous analyses on mollusk shells and coral skeletons have shown that, despite repeated ultrasonic cleanings, alumina is not removed from the surface. To remove contamination due to the polishing step, sections were then etched with 10% formic acid for 5 s, or with 2% acetic acid for 5 s. Previous experiments have shown that etching does not create artifacts (Dauphin & Dufour, 2008).

Micro-Raman Spectroscopy Analyses

Raman spectra were recorded using a Horiba Jobin Yvon LabRam HR 800 spectrometer (Horiba Jobin Yvon SAS, Villeneuve d'Ascq, France) equipped with edge filters, 600 lines/mm grating, an Olympus microscope (Olympus France, Montlhéry, France) equipped with an objective with a magnification factor of 50×, and a Peltier cooled CCD detector. The excitation wavelength was the 458 nm line of an Ar$^+$ laser (Innova 90C, Coherent Inc., Santa Clara, CA, USA). The laser power at the sample was between 2 and 3 mW. The analyzed diameter with the optical set-up used for data collection was about 3 μm.

This configuration led to a spectral resolution of about 2 cm^{-1}, and calibration was checked with respect to the

520.7 cm^{-1} band of silicon. Typical recording times consisted of five accumulations of 3 s.

For mapping, spectra were recorded between 60 and 1,750 cm^{-1}. The acquisition of each spectrum required around 15 s. To investigate spatial distribution of the minerals, the sample was moved by a computer-controlled stage. Each surface was scanned by moving the sample by 5 μm steps. Maps were performed on a 90×500 μm surface for map area 1 (10×5 μm resolution), and 60×500 μm surface for map areas 2 and 3 (5×5 μm resolution). Maps were generated by integrating the area of the band at 277 cm^{-1} (between 236 and 310 cm^{-1}). Spectral acquisitions, baseline subtractions, and map generation were managed by the LabSpec software (Horiba Jobin Yvon SAS, Longjumeau, France) (Horiba Jobin Yvon).

Electron Microprobe Analyses (EDS)

A Zeiss DSM 962 SEM (Carl Zeiss Microscopy Gmbh, Oberkochen, Germany) equipped with an EDAX Falcon X-ray detector system (EDAX Business Unit, AMETEK GmbH, Wiesbaden, Germany) with a 10 mm^2 SUTW window was used for EDS.

The samples (half gastroliths) were mounted on a 45 mm-diameter custom made device and polished to a mirror finish using a series of silicon carbide papers (Struers Gmbh, Willich, Germany) and 100% methanol instead of water to prevent dissolution of amorphous mineral phases.

Spectral maps were recorded from polished air-dried samples coated with a 10 nm-thick layer of carbon at an acceleration voltage of 20 kV and count rates between 1,000 and 2,000 s^{-1}. They were built from these maps employing Genesis software (EDAX).

Because of the water content of the gastroliths, drying inevitably leads to formation of cracks within the polished surface. In principle, these may affect the molar ratios calculated from the spectra. However, since no large signal originates from these cracks in both high and low energy EDX maps, the effect is limited to the edges of the cracks only. Given a number of about ten cracks per millimeter and an excitation depth of only a few micrometer, the effect of the cracks on the calculation of molar ratios is of minor significance.

Micro-XANES Spectroscopy Analyses

This work was carried out at the ID21 beamline of the European Synchrotron Radiation Facility (Grenoble, France). In the ID21 scanning X-ray microscope, a Fresnel zone plate was used as focusing optics to generate a submicron X-ray probe. An energy-dispersive high-purity Ge detector (Princeton Gamma-Tech Instruments, Princeton, NJ, USA) mounted in the horizontal plane perpendicular to the beam collected the fluorescence emission photons. This geometry minimizes the contribution of elastic scattering. An energy range between 2 and 7 keV is available, which gives access to the K-edge of sulfur at 2,472 eV. The XANES energy scan around the sulfur K-edge was achieved using a fixed-exit double-crystal Si(111) monochromator located upstream from the microscope, which offers the necessary energy resolution. This experiment required the X-ray microscope to be operated under vacuum to avoid strong absorption of the sulfur emission lines by air.

Although the primary beam energy was set around that of the S K-edge energy region, elements with absorption edges at lower energies were also subject to excitation and emission of fluorescence photons, and could therefore be determined. Thus, micro-fluorescence element maps of Mg and P were obtained simultaneously with the S maps.

Samples were embedded in resin, and polished using various grades of diamond paste. The oil residue from the diamond paste was removed with a detergent diluted in hot water for 1 min, then rinsed with tap water. Then samples were etched with 1% v/v acetic acid for 5 s, then rinsed with with ultra-pure Milli-Q water (Merck Millipore, Merck KGaA, Darmstadt, Germany) to remove the remaining contaminants. The light etching creates a slightly rough surface, but the height range between hollows and peaks is lower than 5 μm so that the surface is "flat" for non-quantitative analyses. Because fluorescence emission was used as a contrast mechanism, a flat surface of the sample is necessary to avoid signal fluctuations that could have been produced by sample topography. In addition, etching of the sample after polishing helped to eliminate potential surface contamination and remains of the diamond pastes and oil.

Data were normalized and analyzed with the ATHENA program of the IFFEFIT package (Ravel & Newville, 2005).

RESULTS

Light Microscopy and FESEM Observations

The paired gastroliths extracted from a specimen (Fig. 1a) show a hemispherical structure: the flat side corresponds to the beginning of the storage process occurring in between the stomach epithelium and a nonmineralized cuticle underlying this epithelium (Fig. 1d; modified from Travis, 1963). The convex side is the growing side in close contact with epithelial cells. The inner view of a gastrolith, on a fracture as well as on a cross-section, shows a layering structure at different scales (Figs. 1b, 1c). After a slight decalcification treatment on the surface of a gastrolith, the three-dimensional network of chitin-protein fibers is visible (Fig. 1e; Luquet et al., 2013).

FESEM observations confirm the concentric layered pattern, as previously described for different species (Travis, 1960, 1963; Luquet et al., 2013; Habraken et al., 2015). They clearly show rounded structures of around 100-nm diameter, aligned along fibers (Figs. 2a.1, 2a.2). The morphology and size of these spherules (Figs. 2b, 2c) are in accordance with mineralized structures typical of the ACC polymorph (Bentov et al., 2010; Luquet et al., 2013).

Light and SEM microscopy images had previously shown an alternation of layers of different thickness and different levels of brightness (Luquet et al., 2013; see also Fig. 4b). These differences are explained by observations at different magnifications of granular and dense layers (Figs. 3a.1–3a.3). These dense layers, more abundant on the
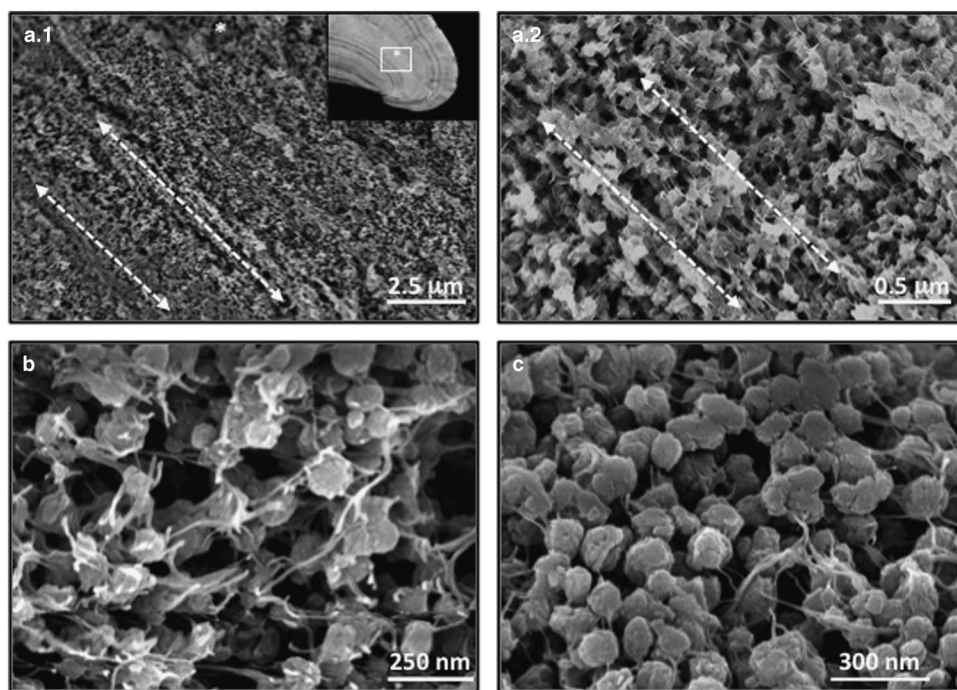
Figure 2. Field emission scanning electron microscopy images of the surface of a naturally broken gastrolith observed on the convex side (end of the storage). **a:** Parallel layers of organic fibers surrounded by mineralized granules are visible [(**a.2**), magnification of (**a.1**)]. **b, c:** Magnifications showing details of the chitin-protein fibers network with nanogranules of around 100-nm diameter.

flat side, seem to correspond to a more or less degree of aggregation of the spherulitic structures (which appear flattened after polishing; Figs. 3b.1–3b.3) observed in the so-called granular layers. Pores are visible in Figure 3b.3 probably corresponding to spaces between fused spherules.

AFM Observations

Figure 4 clearly shows that the layered structure visible at a macroscopic level is also present at a microscopic level (Fig. 4b). The phase contrast image Figure 4c exhibits an alternation of granular (g) and fibrillar (f) layers of around 1 μm thickness. These differences observed after etching may be the result of a difference of richness in organic versus mineral matter of each layer as previously observed after complete decalcification and described in Luquet et al. (2013). Figure 4d is a magnification of a granular area showing irregular aggregated more or less spherical structures (Figs. 4d.1, 4d.2: topographic view, Fig. 4d.3: phase contrast). Figure 4e is a magnification of a zone inside a fibrillar layer. All the phase contrast pictures exhibit clear material, which corresponds to mineralized structures whereas dark regions can be interpreted as organic material.

Fibers of around 5-nm diameter are visible. The original spatial arrangement (alignment of spherules along parallel fibers) seems disrupted following the etching treatment performed before observation.

Figure 5 corresponds to a granular zone. Figures 5b.1, 5c.1, and 5d.1 are height images whereas all the others are

phase contrast images. All the pictures show irregular nanogranules of 50 nm diameter surrounded by dark material. Figure 5e corresponds to a region where the granules are well aligned to each other and along fibers (arrows). These fibers are better visible in Figures 5e.3 and 5f.

Granules are surrounded by a dark cortex in phase images (Fig. 5f, arrowheads). The phase signal changes when the probe encounters regions of different compositions: a soft material is usually "darker" than a hard material (Haugstad, 2012; Mittal & Matsko, 2012). Thus, from these data and what is known about the organo-mineral composition of the samples, it is suggested that the cortex is a mixture of amorphous mineral and organic components (Romano et al., 2007; Thormann et al., 2012).

The biggest granules seem to be the result of fusion/aggregation of single granules of around 50-nm diameter (also visible in Fig. 2c).

The layers richest in fibers are shown at various magnifications in Figure 6. The light color of the fibers, similar to the granules, is probably due to the presence of minerals sheathing these fibers, as described for the chitin-protein fibers of the crustacean cuticle (Romano et al., 2007).

Micro-Raman Spectroscopy Analysis

Raman analyses were performed on particular points on gastrolith cross-sections and by mapping some regions. The spectrum shown in Figure 7a is characteristic of biogenic calcite with peaks at 150, 277, 715, and 1,080 cm^{-1} (Urmos
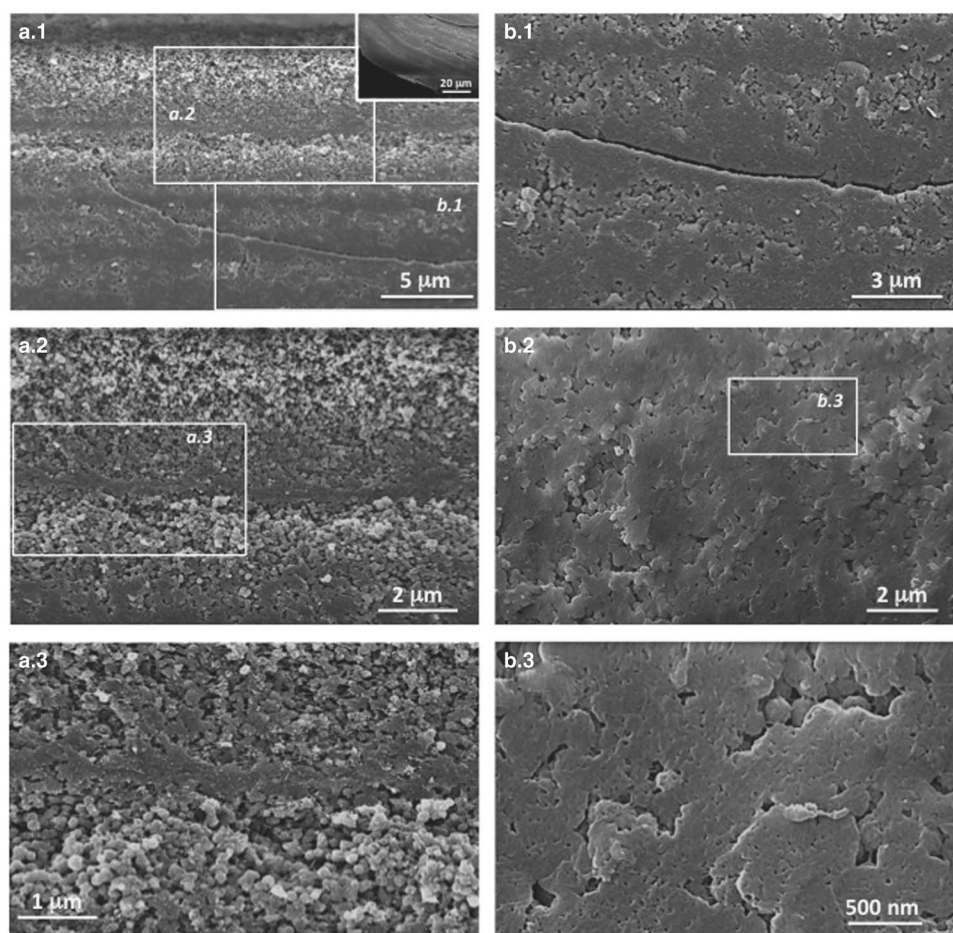
Figure 3. Field emission scanning electron microscopy images of the inner part of a gastrolith, observed on the flat side close to the cuticle (as shown on the insert). **a:** Alternation of bright granular and dark dense layers (**a.1–a.3**: successive magnifications of the same area). **b:** The denser layers are composed of aggregated and fused granules (**b.1–b.3**: different magnifications of a dense layer). Pores visible here correspond to spaces between fused spherules. Rectangles with italics in different pictures indicate the areas that were shown magnified in the corresponding micrographs.

et al., 1991). The strongest band at 1,080 cm^{-1} is an A$_g$ internal mode that derives from the symmetric stretching mode (ν1) of carbonate ions. The peaks visible at 150 and 277 cm^{-1} in map 1 correspond to translational (E$_g$) and rotational (E$_g$) lattice modes of calcite carbonate ions, respectively. The band at 715 cm^{-1} is the internal E$_g$ mode corresponding to the in-plane bending (ν4) mode of calcite carbonate ions. The shift of the main peak from 1,080 cm^{-1} towards 1,077 cm^{-1} in maps b and c is typical of the ACC polymorph (Wehrmeister et al., 2010). Similarly, the only other broad peak observed at 715 cm^{-1} is also characteristic of ACC.

The presence of a faint band at 954 cm^{-1} in the three spectra (Figs. 7a–7c) can be attributed to the presence of phosphate group (ν1 PO$_4$ vibration band, P = O stretching mode; Khan et al., 2013). The shift of the band position observed at 960 cm^{-1} for hydroxyapatite (HAP) and other crystallized calcium phosphates to 954 cm^{-1} can be attributed both to the presence of ACP (Sauer et al., 1994) and to organic phosphated compounds (Bentov et al., 2010). However, this shift could also correspond to the presence of nanocrystalline HAP as suggested (Combes & Rey, 2010).

Raman maps were obtained from three different regions, which means different periods of calcium storage, 1: beginning, 2: middle, 3: end of the process. Maps were obtained by integrating the surface of the band at around 277 cm^{-1} because this band is characteristic of the calcite polymorph of calcium carbonate (spectrum a in Fig. 7). This band is of very low level, almost absent, in the ACC (spectra b and c, Fig. 7). The color of each square, from white (presence) to dark blue (absence), visible on maps 1 (color scale: −3 to 1,300), and 2 (color scale: −10 to 430) is representative of the surface values obtained. The bottom of map 1 corresponds to the limit of the flat region, which means the earlier storage region. We can observe the presence of calcite [spectrum a, white squares/pixels (×a) in maps 1 and 2] and ACC [spectrum b, black squares/pixels (×b) in maps 1 and 2]. Map 2 reveals ACC as the main mineral (dark zones), with layers showing patches of calcite (clear zones). In map 3, whatever the analyzed square (of 5×5 μm) and the color observed (color scale: −3 to 80 to increase contrast), the band at 277 cm^{-1} is virtually undetectable. Spectrum c shows an accumulated spectrum of the 1,100 squares of map 3. All the spectra exhibit
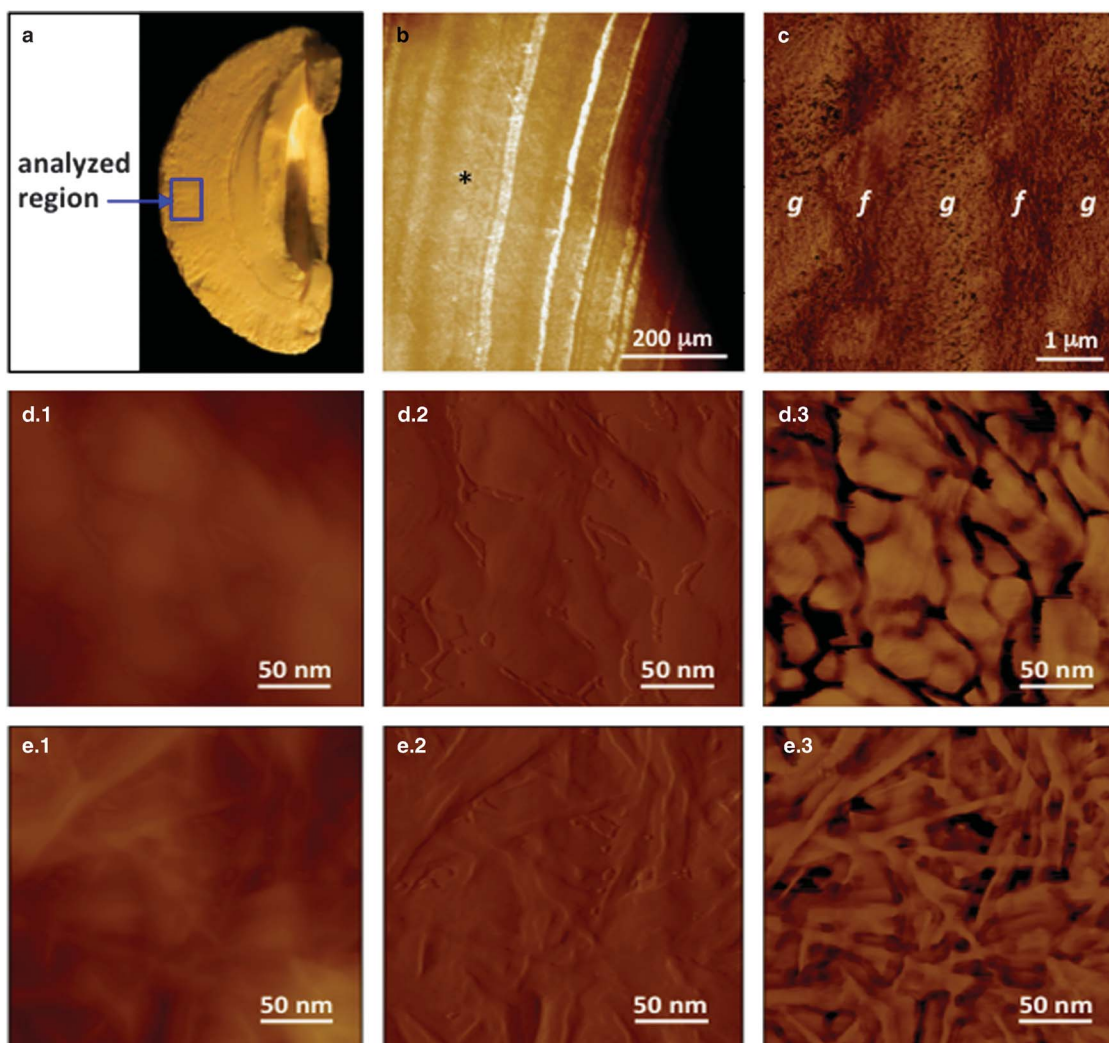
Figure 4. Atomic force microscopy analyses (Tapping mode). **a:** Gastrolith cross-section used for observations after polishing and light etching (light microscopy). **b:** Layered structure visible in the analyzed region (light microscopy; an asterisk indicates the position of the enlarged area shown in Fig. 5). **c:** Phase contrast image showing an alternation of fibrillar (f) and granular (g) layers. **d:** Magnification of a granular area. **e:** Magnification of a fibrillar area. (**d.1**) and (**e.1**): Height images (topography), (**d.2**) and (**e.2**): Amplitude images (chemical interactions), (**d.3**) and (**e.3**): Phase contrast images (chemical composition differences).

only three broad peaks at 715, 954, and 1,077 cm^{-1} with low level variations for each one, which means that the polymorph of calcium carbonate comprising this region is ACC in all areas. We cannot exclude the presence of ACP in a lesser extent in the three different regions because every spectrum exhibits a broad peak at 954 cm^{-1}, putatively indicative of the presence of ACP.

Elemental Composition Analysis

EDS maps of the same cross-section of a gastrolith have been obtained for selected elements. Growth bands are more or less visible in distribution maps (Fig. 8a). Whereas elemental distribution seems homogeneous at this magnification for all the elements except for P, growth layers with a faint heterogeneous distribution are better shown in Figure 8b, an enlargement of part of a gastrolith surface (box in Fig. 8a). On these magnified pictures, the distribution of Ca, O, Na, Fe seems homogeneous

whereas P, S, and Mg have a visible heterogeneous distribution. More particularly a distribution following a subdivision of the thick growth layers (only visible in Fig. 8a) in thinner layers is clearly shown for P (Fig. 8b, arrows). Note that the amount of Fe is very low (Fig. 9b), probably below the limit of detection.

Note that differences in thickness of the growth bands observed in the FESEM images are also visible in the magnified pictures of Figure 8b.

For a better understanding of the topographical relationships between chemical elements, a profile has been done along a transect line in the same region (Fig. 9).

Relative amounts (molar ratio in %) for Ca, P, Mg, and S, are shown along the two lines, a–b and c–d. The beginning of the c–d line, in c, does not coincide exactly with the end of the a–b line, on the b side. If the proportions of magnesium and sulfur rarely exceed 5% along the transect line with a relatively homogeneous distribution, the level of calcium
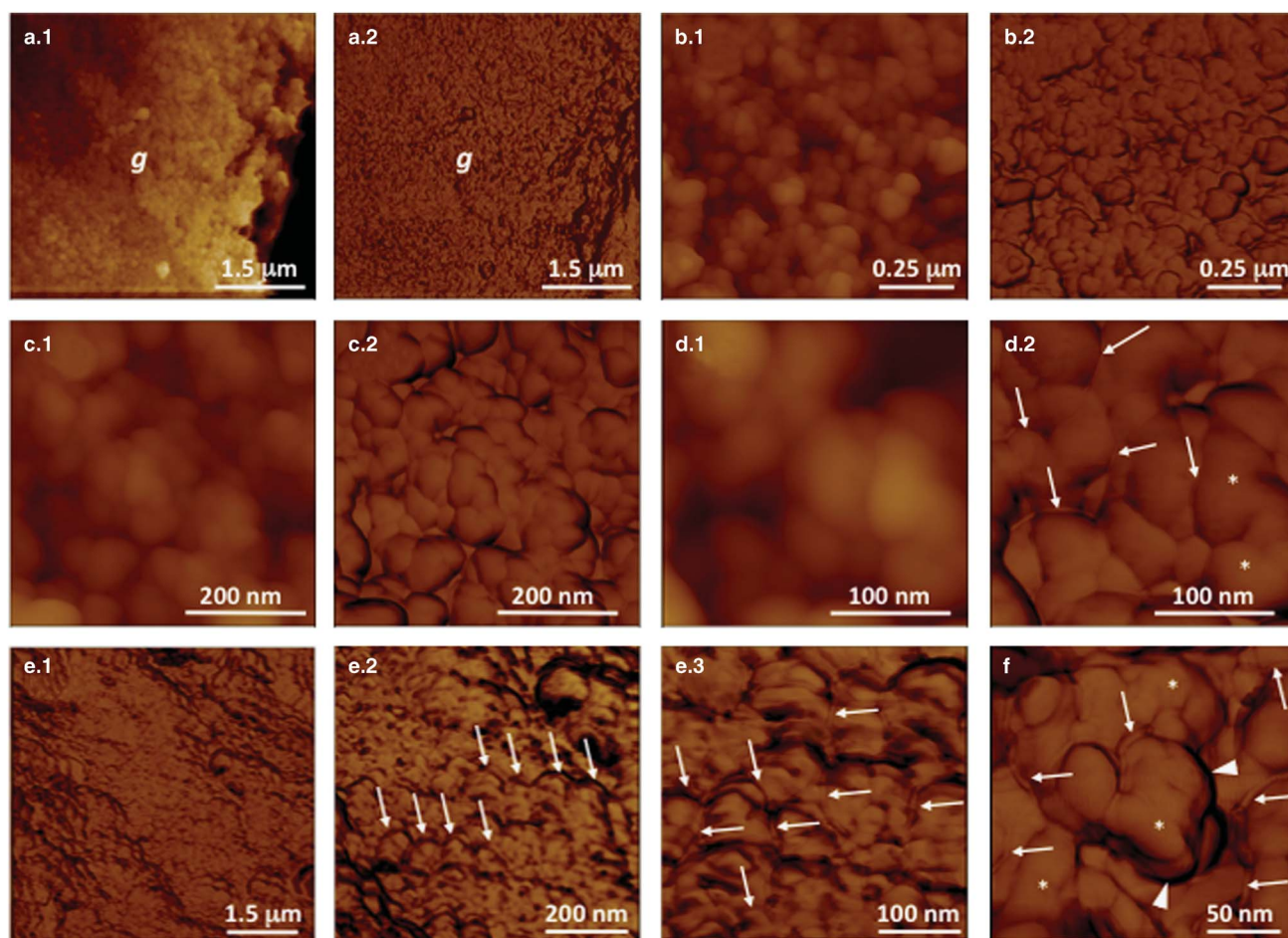
Figure 5. Atomic force microscopy observations of a granular layer (g in Fig. 4c). **a–d:** Series of magnifications of a granular zone where a dense distribution of irregular light nanogranules surrounded by dark material is visible (1: height images, 2: phase contrast images). **e:** Area where granules appear aligned along fibers (as indicated by arrows). **e.1–e.3:** Magnification series of the same area. **f:** High magnification showing clearly fibers (arrows) and dark material (arrowheads). **d.2, f:** * designates aggregated granules of about 50-nm diameter in greater, more or less spherulitic, clusters.

varies by 20 % (between 75 and 95%) depending on the growth layers (Fig. 9a). As for P, relative variations are observed between 4 and 18%. Since the distribution of calcium is more or less homogeneous (Figs. 8a, 8b) the relative changes for calcium and phosphorus are due to the changes in phosphorus. The co-localization of Ca and P and the high P/Ca ratio of up to 0.24 suggest storage of calcium phosphate in addition to calcium carbonate. Regarding the distribution of P (Fig 9a), three regions can be determined: the first, which corresponds to the earlier premolt stage D0, is the center of the initiation of the mineralization process with 4–6% phosphorus (in molar ratio) (Fig. 8a, see the bottom darker region on the phosphorus map). A second region is defined as formed by an alternation of low and higher phosphorus levels from 4–8 to 6–12% (with an increasing rate to 15%). This corresponds to the more layered intermediate gastrolith. The third region has a more homogeneous phosphorus distribution with around 12%-mean molar ratio. The general spectra (Fig. 9b) obtained from two small areas show a similar composition except for P, which is of higher

level in area 2. This area resembles a transition zone where large layers appear concentrated in phosphorus, as also visible in Fig. 8a. This corresponds, in the transect analysis, to the c side (Fig. 9a) where the percent molar ratio is above 15 for P. At the opposite, the d side region (Fig. 9a), corresponding to the beginning of the storage process, seems poor in P.

Micro-XANES Analyses

In organic molecules, sulfur is mainly found associated with proteins or proteoglycans. It is why two sulfur-containing amino acids (cysteine and methionine), cysteine (formed by the oxidization of two cysteines covalently linked via a disulfide bond), and chondroitin sulfate (CS, the most abundant sulfated proteoglycans in living organisms), were used as sulfur-containing organic standards (Fig. 10a). The S K-edge spectra of cysteine and methionine show a main peak at 2,473.5 eV. Cystine displays a characteristic double peak near 2,472.8 and 2,474.3 eV and CS has a main peak at 2,482.7 eV.
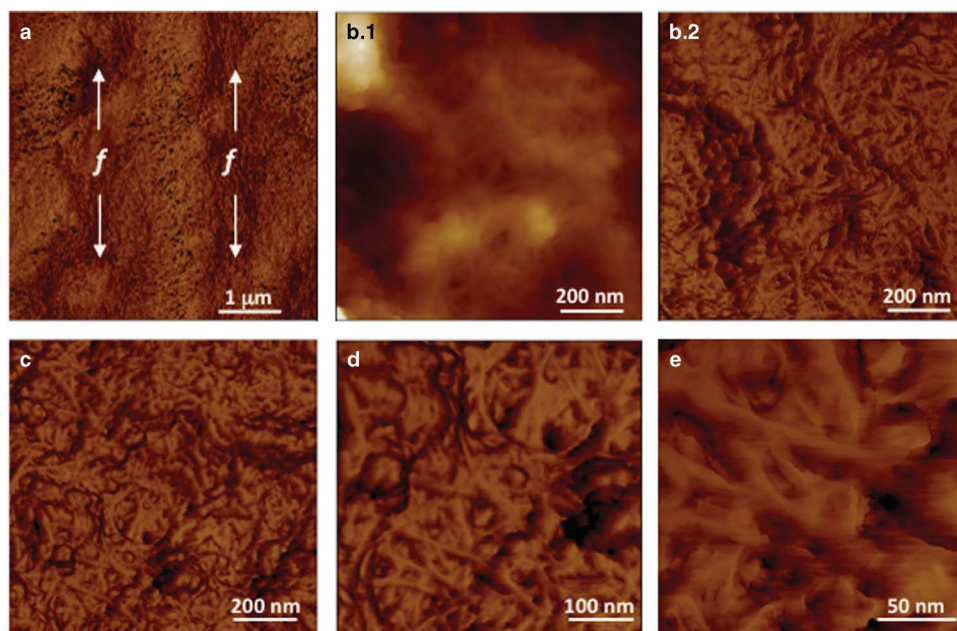
Figure 6. Atomic force microscopy observations of the fibrillar layers. **a:** Analyzed area: alternation of fibrillar (f) and granular layers (phase contrast image). **b:** Magnification of a fibrillar zone; (**b.1**) height image, (**b.2**) phase contrast image. **c–e:** Successive magnifications of the same fibrillar zone after etching (phase contrast images).
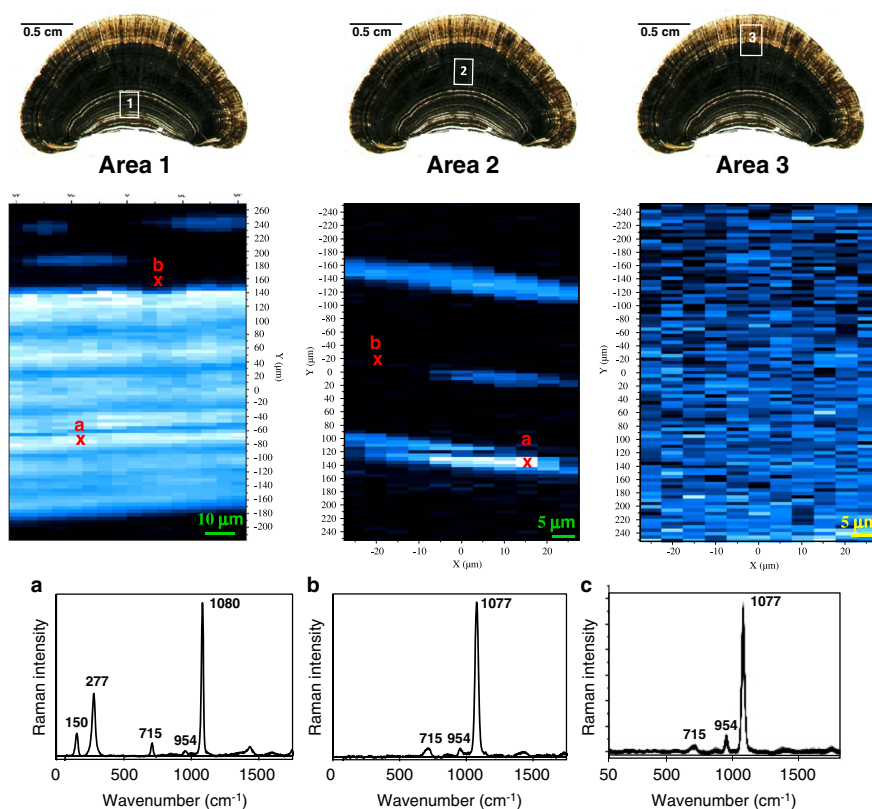
Figure 7. Raman maps and spectra performed on a gastrolith cross-section revealing the mineral composition. Three different areas corresponding to three different periods of storage (inserts above) have been analyzed. Map 1: surface $500 \times 90 \, \mu m$, resolution $5 \, \mu m$, color scale: -3 to $1,300$. Map 2: surface $500 \times 60 \, \mu m$, resolution $5 \, \mu m$, color scale: -10 to 430. Map 3: surface $500 \times 60 \, \mu m$, resolution $5 \, \mu m$, color scale: -3 to 80. Spectrum a, obtained from two white squares on maps 1 and 2 ($\times$a), is typical of calcite. Spectrum b obtained from two dark squares ($\times$b) on maps 1 and 2 corresponds to ACC. Spectrum c shows all the spectra obtained from the 1,110 squares subdividing the analyzed zone: they are all typical of ACC. ACC = amorphous calcium carbonate.
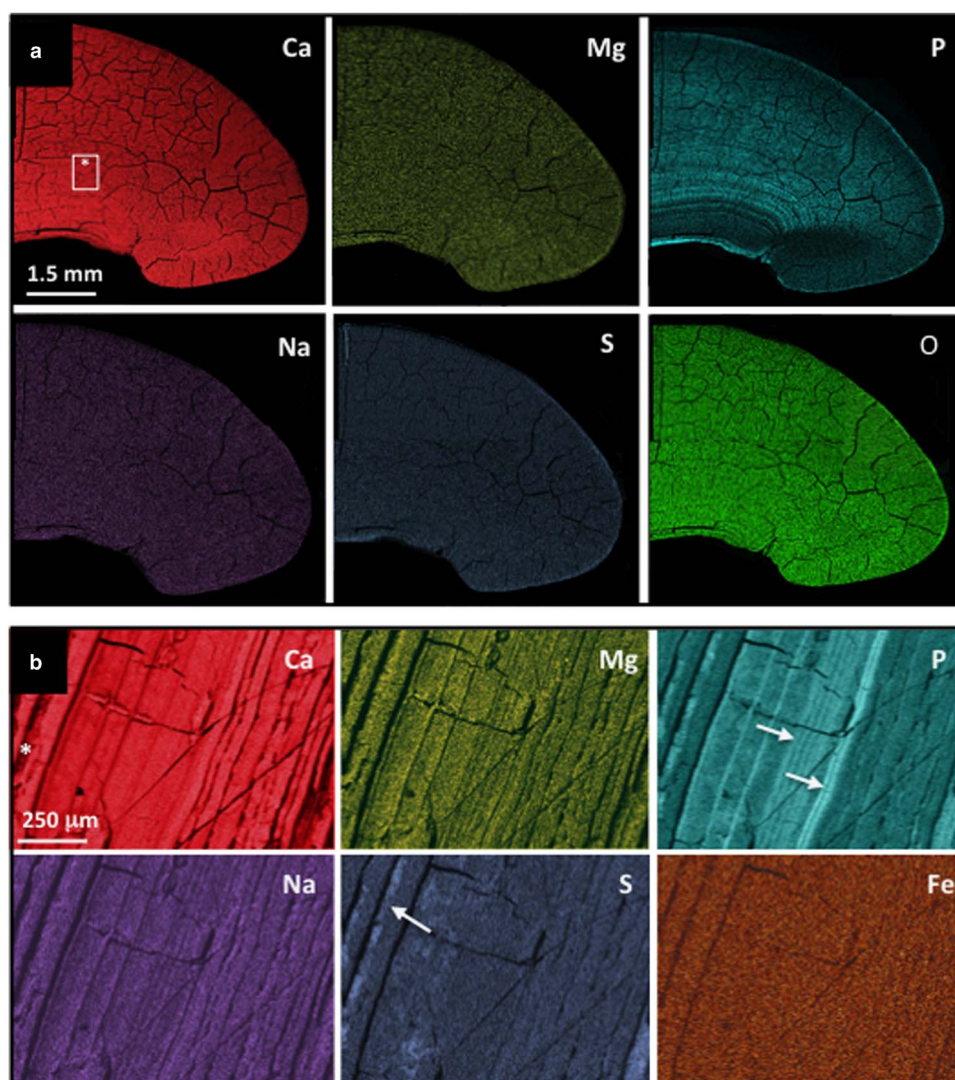
Figure 8. Energy-dispersive X-ray spectroscopy elemental maps showing the distribution of some elements on part of a gastrolith cross-section. **a:** Distribution maps of major and minor elements showing an apparent homogeneous distribution except for P. **b:** Magnification of an area [box in picture (**a**), Ca; an asterisk indicates the corresponding side between the box and the (**b**) rectangular pictures] revealing that the distribution is finely heterogeneous for elements other than P, in relation to the growth layer pattern. The zonal layered distribution is particularly visible for P and S (arrows).

The SOM spectrum (Fig. 10b) exhibits a main peak at 2,481 eV corresponding to sulfonate groups such as $-OSO_3^-$ groups, which can be found for example in proteoglycan sulfate. This peak is also observed as a shoulder in the ascendant part of the mean peak at 2,482.7 found for CS. Moreover, a fit analysis led to the conclusion that the minor peaks observed between 2,473.4 and 2,474 eV correspond to the presence of reduced sulfur, probably in the form of amino acids (R-SH, R-S-CH$_3$). The small shoulder observed on the downslope side of the main peak at 2,482.5 eV corresponds to sulfate. Furthermore, small peaks at 2,476.4 and 2,478.3 eV correspond to the presence, to a lesser extent, of sulfoxide ($R_2S = O$) and sulfite (RSO_3^{2-}), respectively (Pickering et al., 1998; Prietzle et al., 2007).

In situ, the sample spectrum shows characteristics of organic sulfates: a main peak at around 2,482.6 eV (Fig. 10c)

and the second part of the spectrum is similar to that of CS. Minor peaks at 2,473.2 and 2,474.4 eV are due to the presence of reduced sulfur similar to that present in amino acids (cysteine and methionine). The right part of the spectrum is similar to the large shoulder of the CS profile.

From these spectra, it can be concluded that molecules containing sulfate groups similar to those found in sulfated glycosaminoglycans are the principal organosulfur compounds whereas S-containing amino acids are of low abundance. Sulfur is also present in other chemical states (sulfite, sulfoxide, sulfonate), as a minor contribution.

Micro-fluorescence maps (Fig. 10d) show similar results and correlate well with the electron microprobe maps obtained. The most interesting feature of the XANES maps can be seen in the map acquired at the sulfate peak energy that shows zonations. The map at energy 2,437.5 eV
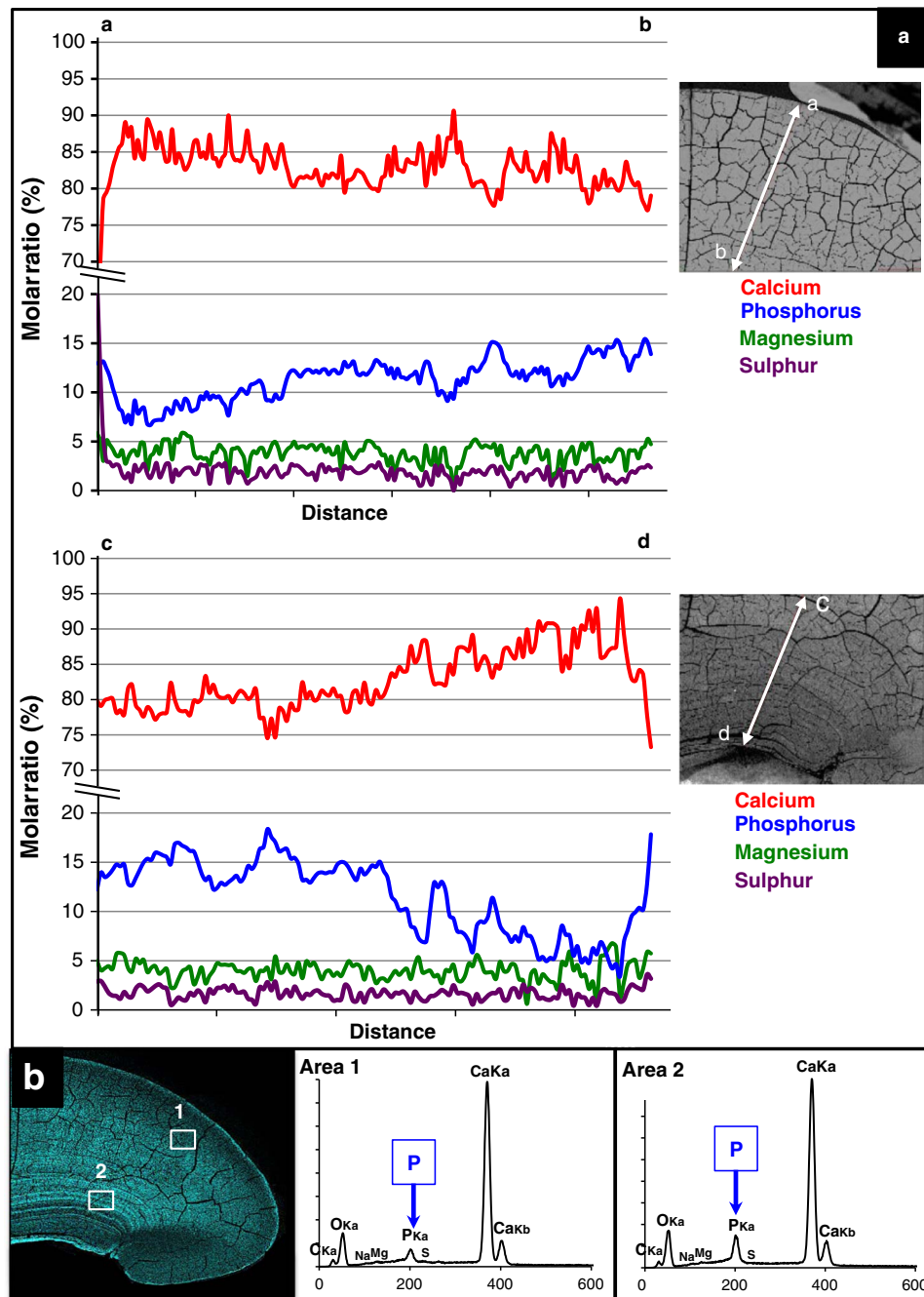
Figure 9. Energy-dispersive X-ray spectroscopy analysis. **a:** At left, molar ratio % obtained for Ca, P, S, and Mg along transect lines shown at right (scanning electron microscopy images of two analyzed zones of the sample shown in Fig. 8. **a:** On which the position of the transect lines is indicated). **b:** Spectra obtained for two different small areas showing the relative concentration of different elements. Only the P concentration seems variable from one area to the other.

(Fig. 10c, S aa) corresponds to the distribution of S from the amino acids cysteine/cystine and methionine. Due to the weak signal, no clear zonation is seen.

DISCUSSION

The layering structure of gastroliths from crayfish was first evidenced on *Orconectes virilis* (Travis, 1960). The layered

structure of *C. quadricarinatus* gastroliths was previously observed (Shechter et al., 2008a; Luquet et al., 2013), but nothing is clear about width and composition differences of the layers in relation with different light reactivities (brightness, transparency, …). A similar organization was also observed by Habraken et al. (2015) on a crayfish. Unfortunately, the name of the genus and species of which is not given in the study, so that detailed comparisons are difficult. Because
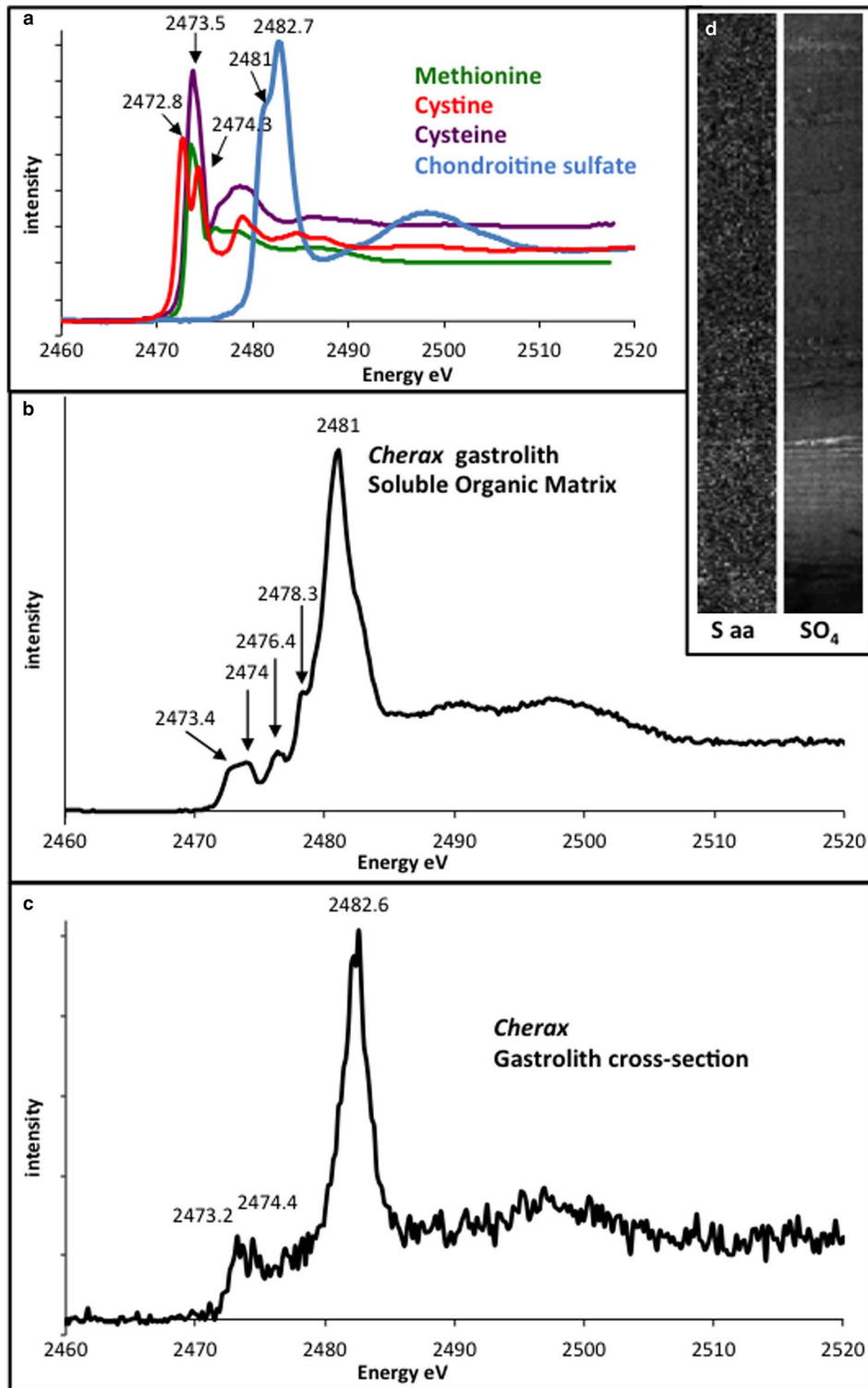
Figure 10. XANES analysis. **a:** XANES S spectra from organic sulfated components: chondroitin sulfate showing a main peak at 2.483 keV and sulfated amino acid standards showing a main peak at 2.473 keV. **b:** Spectrum obtained on a soluble organic matrix extract. **c:** Spectrum obtained *in situ* on a small area of a gastrolith cross-section. **d:** Micro-XANES maps—sulfur speciation. XANES maps showing the abundance of S and organic sulfate (SO_4) in relation with the growth layer pattern. XANES = X-ray absorption near edge structure spectroscopy.

of differences in the composition between gastroliths from different species, as previously described (Luquet et al., 2013), it is of great importance to provide this information.

FESEM observations clearly show that the inner gastrolith structure of *C. quadricarinatus* is composed of nanogranules aligned along mineralized fibers. Furthermore, FESEM

pictures also reveal that some layers result in the aggregation of nanogranules in a denser and more homogenous structure as also shown by Habraken et al. (2015). This type of denser layer appears more abundant on the flat side (earlier storage region) of the gastrolith than in the latter convex storage zone. Analogous calcium deposits, the sternal plates, synthesized by terrestrial isopods such as the woodlice *Porcellio scaber*, *Ligidium hypnorum*, and *Armadillidium vulgare*, exhibit similar agglomerated zones depending on the species from an evolutionary viewpoint (Ziegler & Miller, 1997; Ziegler et al., 2005). It could be linked to the need to store more and more calcium during the terrestrialization of isopods in relation to the thickening of the cuticle. This aspect has not been investigated so far for gastrolith-forming decapods.

AFM analyses show the presence of alternating granular-rich and fibrillar-rich layers. This corresponds to the previously observed richness differences in chitin-protein fibers forming meshes of different sizes filled with $CaCO_3$ (see Figs. 3d, 3e in Luquet et al., 2013). The smallest granules are of 50-nm mean diameter for the majority of them. Fibers are also visible, the light aspect of which suggests they are mineralized. Some granules seem furthermore surrounded by material probably of organic origin. We also observed aggregations of granules in largest structures more or less spherulitic that vary in size from 100 to 200 nm. This is in accordance with the two-step mode of growth theory previously described for other calcareous crystalline biominerals (Cuif & Dauphin, 2005; Cuif et al., 2008, 2012). This suggests that this mode of growth is probably universal whatever the nature of the mineral, crystalline, or amorphous, as is the layered mode of growth (Cuif et al., 2012).

Micro-Raman analyses reveal the presence of calcium carbonate as ACC and calcite and probably also calcium phosphate as ACP. Calcite seems restricted to the first storage region where dense layers are observed. Its presence *in vivo* cannot be ascertained. It has been known for a long time that the local chemical environment, as well as availability of specific molecules and mineral ions, are fundamental in the development of a biomineral (Mann, 1983; Lowenstam & Weiner, 1989). This is the case for such ACC-stabilized gastroliths. The presence of calcite could be here the effect of a secondary crystallization process resulting from the exposure of such an ACC-biomineral to air atmosphere during dissection and sample preparation. It has been previously demonstrated that, during experimentation, exposure to different conditions (of humidity notably) than the environmental *in vivo* conditions could induce such a recrystallization process (Raz et al., 2002; Luquet et al., 2013; Reeder et al., 2013). It has been notably mentioned that, in aged gastroliths, calcite, vaterite, and trace amounts of monetite ($CaHPO_4$) are detected (Reeder et al., 2013). We must notice nevertheless that only the earlier synthesized zone of a gastrolith is affected by the presence of calcite, whereas ACC and ACP seem present everywhere in the gastrolith.

The spatial distribution of some elements corroborates the layered pattern. P and S for example are clearly heterogeneously distributed.

The presence of phosphorus in gastroliths was first demonstrated by Travis (1963) in *Orconectes limosus*. Its presence was observed everywhere in the gastrolith, with a mean amount increasing from 1.2% (by dry weight) in the "young" gastrolith to about 1.6% in the fully developed gastrolith of *O. limosus*. Whatever the molecular form in which phosphorus is present in gastroliths, EDS analyses here in *Cherax* suggest that its level is richer in layers of the earlier zone, but its distribution is more homogenous in the latter storage region. The origin of this phosphorus, from organic molecules or from the inorganic phase, has not been evidenced here. Nevertheless, Raman analyses suggest the presence of ACP in the mineral phase of gastroliths.

Gastrolith ACP cannot be considered as a reservoir of phosphorus available for the carbonate apatite teeth because their mineralization occurs in premolt concomitantly with gastrolith formation (Bentov et al., 2012). However, P can be used for the postmolt mineralization of parts of the cuticle where ACP has been clearly evidenced in decapods (Soejoko & Tjia, 2003; Fabritius et al., 2012; Kunkel & Jercinovic, 2013). It was previously observed that other decapods, which do not develop gastroliths, store calcium in other storage sites, such as the hepatopancreas or the hemolymph, along with phosphate ions used for the mineralization of each new cuticle (Robertson, 1937; Travis, 1955; Sparkes & Greenaway, 1984). Isopods also cyclically store calcium phosphate in sternal deposits or in inner storage bodies for the mineralization of their new exoskeleton comprising ACP (Ziegler, 2003).

P has been also observed in organic molecules. Phosphorylated proteins have been characterized and hypothesized as playing a role in ACC stabilization (Shechter et al., 2008b; Bentov et al., 2010; Glazer et al., 2010). On the other hand, small phosphorylated metabolites have also been observed by NMR and thought to play an interacting role between matrix proteins and calcium ions (Akiva-Tal et al., 2011; Sato et al., 2011). The presence of phosphorus in high level shown by Raman and EDS analyses seems then logical and can be related to such a function in addition to phosphate ion storage needed for mineralization of the new cuticle. It has been previously strongly suggested (Bentov et al., 2010; Habraken et al., 2015) that phosphorylated molecules are mainly responsible for the stabilization of ACC calcium carbonate, but in a different mixing composition and concentration from one layer to another. *In vitro* experiments performed by Hennig et al. (2012) demonstrated that phosphate compounds are not required for ACC formation/stabilization by *P. scaber* soluble matrix unphosphorylated proteins.

The presence of sulfur is not surprising because it seems commonly found in most of the carbonated biominerals. For example, it has been found in corals (Cuif et al., 2003; Dauphin et al., 2008; Zhang et al., 2011), mollusks (Dauphin et al., 2003, 2005; Rousseau et al., 2009), and brachiopods (Cusack et al., 2008). It was also detected in avian eggshells (Dauphin et al., 2006). In most cases, sulfur as sulfate groups seems associated to sugars or glycosaminoglycans as suggested also for gastroliths. The presence of sulfonate groups

R–SO2OH could correspond to S linked to carbohydrates or to the sugar domain of proteoglycans (O-sulfonated glycosaminoglycans). Sulfate groups can be also associated with glycosylated proteins containing sulfated sugar moieties. Carbohydrates and proteoglycans have been found in gastroliths (Fernandez et al., 2012; Luquet et al., 2013).

A role of acidic glycoproteins (possibly sulfated) in the control of nucleation and growth as well as inhibition of crystallization has been suggested (Wheeler et al., 1981; Addadi et al., 1996; Albeck et al., 1996).

Inorganic sulfate can also be incorporated in the mineral bulk in place of carbonate ions, but most often in association with calcite (Busenberg & Plummer, 1985; Kontrec et al., 2004). If the presence of calcite in gastrolith was detected by Raman spectroscopy, it could be the result of an experimental recrystallization process. Its real presence *in vivo* cannot be asserted.

Travis (1963) described three developmental steps of *O. virilis* gastrolith formation resulting in a "young, intermediate, and mature" gastrolith. Microscopy, Raman, and EDS results, obtained for *C. quadricarinatus* gastroliths, corroborate these conclusions: three distinct regions can be defined in a mature gastrolith. The first region, which corresponds to the beginning of the storage (flat side) exhibits denser layers, with mainly calcite, but also ACC and ACP and with a low level of phosphorus. The second intermediate region presents mainly ACC, and lesser calcite and ACP with the higher content of phosphorus increasing from the beginning of the gastrolith synthesis. The third region (convex side, end of storage) appears less densely packed, more regularly layered with separated nanogranules of ACC and probably also phosphate as ACP, with a regular intermediary level of phosphorus.

The reason for this spatial/temporal organization is not well established. It could be related to three different periods of storage occurring during the premolt. The "softer" last-synthesized region could coincide with an increase of the two concomitant processes, decalcification of the endocuticle and mineral ion storage, as ecdysis approaches (Travis, 1963). This was previously well established for other storage deposits elaborated in the terrestrial amphipod, *Orchestia cavimana* (Testeniere et al., 2012). It could also correspond to a part of the gastrolith more easily and quickly mobilizable after ecdysis. Just after ecdysis, these deposits collapse in the gastric lumen where they are completely dissolved within 2–3 days. The real cuticular targets of the reused calcium ions have not been clearly determined. Nevertheless, it is generally considered that gastrolith calcium, which represents from 4–7 (in *Austropotamobius pallipes*) to 18% (in *Procambarus clarkii*) of the complete intermolt skeleton calcium amount, is preferentially used to harden mouthparts and the gastric mill so that feeding can resume (Ryhänen, 1962; Chaisemartin, 1964; Graf, 1978; Greenaway, 1985).

Conclusions

The layered structure of a gastrolith can be related to its elemental composition. The distribution of some elements seems closely related to the spatial-temporal events of organic synthesis concomitant to the mineralization process.

The most abundant secondary element (after C, O, and Ca), phosphorus, because of its general spatial distribution observed by EDS and XANES, appears to be incorporated as an element of both mineral and organic compounds all during the synthesis of gastroliths. Therefore, it is probably an important element at various steps of gastrolith formation, as previously evoked (Travis, 1963; Bentov et al., 2010; Akiva-Tal et al., 2011; Sato et al., 2011; Luquet, 2012; Habraken et al., 2015). If ACP and phosphorylated proteins are present, further investigations are necessary to clearly identify the nature of all the phosphorus-composed molecules and their distribution linked to their function in the formation of these cyclically synthesized and resorbed calcified deposits.

The presence of sulfur clearly shown here seems mainly related to sulfated organic components, more especially with sulfated sugars and, to a lesser extent, with amino acids containing sulfur. Their distribution appears relatively homogeneous, but the real function of these molecules has not been clearly deciphered. As phosphorylated molecules, they could be involved in interactions with calcium ions promoting or preventing the crystallization process of $CaCO_3$.

For explaining ACC stabilization over time in gastroliths, a mixed repertoire of interacting compounds is probably necessary. Besides previously observed low-molecular weight metabolites (citrate, PEP), Mg and sulfate and phosphate groups probably linked to proteins and sugars were found. Their respective involvement in the control of gastrolith formation remains to be determined, as does their involvement in the pathway leading to inhibition of the crystallization process in a way that allows perennial stabilization of the mineral phase in an amorphous form.

References

Addadi, L., Moradian, J., Shay, E., Maroudas, M.G. & Weiner, S. (1987). A chemical model for the cooperation of sulfates and carboxylates in calcite crystal nucleation: Relevance to biomineralization. *Proc Natl Acad Sci USA* **84**, 2732–2736.

Addadi, L., Raz, S. & Weiner, S. (2003). Taking advantage of disorder: Amorphous calcium carbonate and its role in biomineralization. *Adv Mater* **15**, 959–970.

AIZENBERG, J., LAMBERT, G., WEINER, S. & ADDADI, L. (2001). Factors involved in the formation of amorphous and crystalline calcium carbonate: A study of an ascidian skeleton. *J Am Chem Soc* **124**, 32–39.

AKIVA-TAL, A., KABAYA, S., BALAZS, Y.S., GLAZER, L., BERMAN, A., SAGI, A. & SCHMIDT, A. (2011). *In situ* molecular NMR picture of bioavailable calcium stabilized as amorphous CaCO₃ biomineral in crayfish gastroliths. *Proc Natl Acad Sci USA* **108**, 14763–14768.

ALBECK, S., ADDADI, L. & WEINER, S. (1996). Regulation of calcite crystal morphology by intracrystalline acidic proteins and glycoproteins. *Connect Tissue Res* **35**, 365–370.

BECKER, A., ZIEGLER, A. & EPPPLE, M. (2005). The mineral phase in the cuticles of two species of Crustacea consists of magnesium calcite, amorphous calcium carbonate, and amorphous calcium phosphate. *Dalton Trans*, 1814–1820.

BENTOV, S., WEIL, S., GLAZER, L., SAGI, A. & BERMAN, A. (2010). Stabilization of amorphous calcium carbonate by phosphate rich organic matrix proteins and by single phosphoamino acids. *J Struct Biol* **17**, 207–215.

BENTOV, S., ZASLANSKY, P., AL-SAWALMIH, A., MASIC, A., FRATZL, P., SAGI, A., BERMAN, A. & AICHMAYER, B. (2012). Enamel-like apatite crown covering amorphous mineral in a crayfish mandible. *Nat Commun* **3**, 839–845.

BLISS, D.E. (1953). Endocrine control of metabolism in the land crab, *Gecarcinus lateralis* (Freminville). I. Differences in the respiratory metabolism of sinusglandless and eyestalkless crabs. *Biol Bull* **104**, 275–296.

BUSENBERG, E. & PLUMMER, L.N. (1985). Kinetic and thermodynamic factors controlling the distribution of SO₄²⁻ and Na⁺ in calcites and selected aragonites. *Geochim Cosmochim Acta* **49**, 713–725.

CHAISEMARTIN, C. (1964). Importance des gastrolithes dans l'économie du calcium chez *Astacus pallipes* (Lereboullet). Bilan calcique de l'exuviation. *Vie Milieu* **15**, 457–474.

CHANTRAN, M.S. (1874). Observations sur la formation des pierres chez les écrevisses. *C R Acad Sci Paris* **78**, 6555–6557.

COMBES, C. & REY, C. (2010). Amorphous calcium phosphates: Synthesis, properties and uses in biomaterials. *Acta Biomater* **6**, 3362–3378.

CUIF, J.P. & DAUPHIN, Y. (2005). The two-step mode of growth in the scleractinian coral skeletons from the micrometre to the overall scale. *J Struct Biol* **150**, 319–331.

CUIF, J.P., DAUPHIN, Y., DOUCET, J., SALOME, M. & SUSINI, J. (2003). XANES mapping of organic sulfate in three scleractinan coral skeletons. *Geochim Cosmochim Acta* **67**, 75–83.

CUIF, J.-P., DAUPHIN, Y., FARRE, B., NEHRKE, G. & NOUET, J. (2008). Distribution of sulfated polysaccharides within calcareous biominerals suggests a widely shared two-step crystallization process for the microstructural growth units. *Mineral Mag* **72**, 233–237.

CUIF, J.-P., DAUPHIN, Y., FARRE, B., NEHRKE, G., NOUET, J. & PEREZ-HUERTA, A. (2012). Layered growth and crystallization in calcareous biominerals: Impact of structural and chemical evidence on two major concepts in invertebrate biomineralization studies. *Minerals* **2**, 11–39.

CUSACK, M., DAUPHIN, Y., CUIF, J.P., SALOME, M., FREER, A. & YIN, H. (2008). Micro-XANES mapping of sulfur and its association with magnesium and phosphorus in the shell of the brachiopod, *Terebratulina retusa*. *Chem Geol* **253**, 172–179.

DAUPHIN, Y., CUIF, J.P., DOUCET, J., SALOME, M., SUSINI, J. & WILLIAMS, T. (2003). *In situ* chemical speciation of sulfur in calcitic biominerals and the simple prism concept. *J Struct Biol* **142**, 272–280.

DAUPHIN, Y., CUIF, J.P., SALOME, M. & SUSINI, J. (2005). Speciation and distribution of sulfur in a mollusk shell as revealed by *in situ* maps using X-ray absorption near-edge structure (XANES) spectroscopy at the SK-edge. *Am Mineral* **90**, 1748–1758.

DAUPHIN, Y., CUIF, J.P., SALOME, M., SUSINI, J. & WILLIAMS, T. (2006). Microstructure and chemical composition of giant avian eggshells. *Anal Bioanal Chem* **386**, 1761–1771.

DAUPHIN, Y., CUIF, J.P. & WILLIAMS, T. (2008). Soluble organic matrices of aragonitic skeletons of *Merulinidae* (Cnidaria, Anthozoa). *Comp Biochem Physiol B* **150**, 10–22.

DAUPHIN, Y. & DUFOUR, E. (2008). Nanostructures of the aragonitic otolith of cod (*Gadus morhua*). *Micron* **39**, 891–896.

DILLAMAN, R., HEQUEMBOURG, S. & GAY, M. (2005). Early pattern of calcification in the dorsal carapace of the blue crab, *Callinectes sapidus*. *J Morphol* **263**, 356–374.

FABRITIUS, H.-O., BALASUNDARAM, E.S., HILD, S., HUEMER, K. & RAABE, D. (2012). Correlation of structure, composition and local mechanical properties in the dorsal carapace of the edible crab *Cancer pagurus*. *Z Kristallog Kristallgeom Kristallphysic Kristallchem* **227**, 766–776.

FARMER, A.S. (1973). Age and growth in *Nephrops norvegicus* (Decapoda: Nephropoidae). *Mar Biol* **23**, 315–325.

FERNANDEZ, M.S., BUSTOS, C., LUQUET, G., SAEZ, D., NEIRA-CARRILLO, A., CORNEILLAT, M., ALCARAZ, G. & ARIAS, J.L. (2012). Proteoglycan occurrence in gastrolith of the crayfish *Cherax quadricarinatus* (Crustacea, Malacostraca, Decapoda). *J Crust Biol* **32**, 802–815.

GLAZER, L. & SAGI, A. (2012). On the involvement of proteins in the assembly of the crayfish gastrolith extracellular matrix. *Invert Rep Dev* **56**, 57–65.

GLAZER, L., SHECHTER, A., TOM, M., YUDKOVSKI, Y., WELL, S., AFLALO, E.D., PAMURU, R.R., KHALAILA, I., BENTOV, S., BERMAN, A. & SAGI, A. (2010). A protein involved in the assembly of an extracellular calcium storage matrix. *J Biol Chem* **285**, 12831–12839.

GLAZER, L., TOM, M., WEIL, S., ROTH, Z., KHALAILA, I., MITTELMAN, B. & SAGI, A. (2013). Hemocyanin with phenoloxidase activity in the chitin matrix of the crayfish gastrolith. *J Exp Biol* **216**, 1898–1904.

GRAF, F. (1978). Les sources de calcium pour les crustacés venant de muer. *Arch Zool Exp Gen* **119**, 143–161.

GREENAWAY, P. (1985). Calcium balance and molting in the Crustacea. *Biol Rev* **60**, 425–454.

GRUNENFELDER, L.K., HERRERA, S. & KISALIUS, D. (2014). Crustacean-derived biomimetic components and nanostructured composites. *Small* **16**, 30207–30232.

HABRAKEN, W.J.E.M., MASIC, A., BERTINETTI, L., AL-SAWALMIH, A., GLAZER, L., BENTOV, S., FRATZL, P., SAGI, A., AICHMAYER, B. & BERMAN, A. (2015). Layered growth of crayfish gastrolith: About the stability of amorphous calcium carbonate and role of additives. *J Struct Biol* **189**, 28–36.

HAN, T.Y.-J. & AIZENBERG, J. (2008). Calcium carbonate storage in amorphous form and its template-induced crystallization. *Chem Mater* **20**, 1064–1068.

HAUGSTAD, G. (2012). *Atomic Force Microscopy: Understanding Basic Modes and Advanced Applications*. Hoboken, NJ, USA: John Wiley & Sons.

HENNIG, S., HILD, S., FABRITIUS, H.-O., SOOR, C. & ZIEGLER, A. (2012). Influence of near-physiological salines and organic matrix proteins from amorphous CaCO₃ deposits of *Porcellio scaber* on *in vitro* CaCO₃ precipitation. *Cryst Growth Des* **12**, 646–655.

HERRICK, F.H. (1911). *Natural History of the American Lobster.* Cambridge: U.S. Government Printing Office, Harvard University Press.

HIKIDA, T., NAGASAWA, H. & KOGURE, T. (2003). Characterization of amorphous calcium carbonate in the gastrolith of crayfish, *Procambarus clarkii.* In *Biomineralization: Formation, Diversity, Evolution and Application*, Kobayashi, I. & Ozawa, H. (Eds.), pp. 81–84. Kanagawa: Tokai University Press.

HUXLEY, T.H. (1879). *The Crayfish: An Introduction to the Study of Zoology. The International Scientific Series*, vol. XXVIII. London, UK: C. Kegan Paul & Company, Oxford University Press.

ISHII, K., YANAGISAWA, T. & NAGASAWA, H. (1996). Characterization of a matrix protein in the gastroliths of the crayfish *Procambarus clarkii. Biosci Biotechnol Biochem* **60**, 1479–1482.

KHAN, A.F., AWAIS, M., KHAN, S.A, TABASSUM, S., CHAUDHRY, A.A. & REHMAN, I.U. (2013). Raman spectroscopy of natural bone and synthetic apatites. *Appl Spectrosc Rev* **48**, 329–355.

KONTREC, J., KRALJ, D., BRECEVIC, L., FALINI, G., FERMANI, S., NOETHIG-LASLO, V. & MIROSAVLJEVIC, K. (2004). Incorporation of inorganic anions in calcite. *Eur J Inorg Chem* **2004**, 4579–4595.

KUGLER, O.E. & BIRKNER, M.L. (1948). Histochemical observations of alkaline phosphatase in the integument, gastrolith sac, digestive gland and nephridium of the crayfish. *Physiol Zool* **21**, 105–110.

KUNKEL, J.G. & JERCINOVIC, M.J. (2013). Carbonate apatite formulation in cuticle structure adds resistance to microbial attack for American lobster. *Mar Biol Res* **9**, 27–34.

LOSTE, A., WILSON, R.M., SESHADRIC, R. & MELDRUM, F.C. (2003). The role of magnesium in stabilising amorphous calcium carbonate and controlling calcite morphologies. *J Cryst Growth* **254**, 206–208.

LOWENSTAM, H.A. & WEINER, S. (1989). *On Biomineralization.* London, UK: Oxford University Press.

LUQUET, G. (2012). Biomineralizations: Insights and prospects from crustaceans. *Zookeys* **176**, 103–121.

LUQUET, G., FERNANDEZ, M.S., BADOU, A., GUICHARD, N., LE ROY, N., CORNEILLAT, M., ALCARAZ, G. & ARIAS, J.L. (2013). Comparative ultrastructure and carbohydrate composition of gastroliths from Astacidae, Cambaridae and Parastacidae freshwater crayfish (Crustacea, Decapoda). *Biomolecules* **3**, 18–38.

LUQUET, G., LE ROY, N., ZANELLA-CLÉON, I., BECCHI, M., BUCAREY, S., FERNANDEZ, M.S., ARIAS, J.L., GUICHARD, N., MARIE, B. & MARIN, F. (2009). Characterization of crustacyanin-A2 subunit as a component of the organic matrix of gastroliths from the crayfish *Cherax quadricarinatus. Mater Res Soc Symp Proc* **1187**, 69–75.

LUQUET, G. & MARIN, F. (2004). Biomineralizations in crustaceans: Storage strategies. *C R Palevol* **3**, 515–534.

MANN, S. (1983). Mineralization in biological systems. *Struct Bond* **54**, 125–174.

MITTAL, V. & MATSKO, N.B. (2012). *Analytical Imaging Techniques for Soft Matter Characterization.* New York, NY, USA: Springer Science & Business Media.

NEUES, F., ZIEGLER, A. & EPPLE, M. (2007). The composition of the mineralized cuticle in marine and terrestrial isopods: A comparative study. *Cryst Eng Comm* **9**, 1245–1251.

NUMANOI, H. (1939). Behavior of blood calcium in the formation of gastroliths in some decapod crustaceans. *Jap J Zool* **8**, 357–363.

PICKERING, I.J., PRINCE, R.C., DIVERS, T. & GEORGE, G.N. (1998). Sulfur K-edge X-ray absorption spectroscopy for determining the chemical speciation of sulfur in biological systems. *FEBS Lett* **441**, 11–14.

POLITI, Y., METZLER, R.A., ABRECHT, M., GILBERT, B., WILT, F.H., SAGI, I., ADDADI, L., WEINER, S. & GILBERT, P.U. (2008). Transformation mechanism of amorphous calcium carbonate into calcite in the sea urchin larval spicule. *Proc Natl Acad Sci USA* **105**, 17362–17366.

PRIETZEL, J., THIEME, J., SALOME, M. & KNICKER, H. (2007). Sulfur K-edge XANES spectroscopy reveals differences in sulfur speciation of bulk soils, humic acid, fulvic acid and particle size separates. *Soil Biol Biochem* **39**, 877–890.

RAVEL, B. & NEWVILLE, M. (2005). ATHENA, ARTEMIS, HEPHAESTUS: data analysis for X-ray absorption spectroscopy using IFEFFIT. *J Synchrotron Rad* **12**, 537–541.

RAZ, S., HAMILTON, P., WILT, F., WEINER, S. & ADDADI, L. (2003). The transient phase of amorphous calcium carbonate in sea urchin spicules: The involvement of proteins and magnesium ions in their formation and stabilization. *Adv Funct Mater* **13**, 480–486.

RAZ, S., TESTENIERE, O., HECKER, A., WEINER, S. & LUQUET, G. (2002). Stable amorphous calcium carbonate is the main components of the calcium storage structures of the crustacean *Orchestia cavimana. Biol Bull* **203**, 269–274.

REEDER, R.J., TANG, Y., SCHMIDT, D.T., KUBISTA, L.M., COWAN, D.F. & PHILIPS, B.L. (2013). Characterization of structure in biogenic amorphous calcium carbonate: Pair distribution function and nuclear magnetic resonance studies of lobster gastrolith. *Cryst Growth Des* **13**, 1905–1914.

ROBERTSON, J.D. (1937). Some features of calcium metabolism of the shore crab (*Carcinus maenas* Pennant). *Proc Roy Soc London B* **124**, 162–182.

ROMANO, P., FABRITIUS, H. & RAABE, D. (2007). The exoskeleton of the lobster, *Homarus americanus*, as an example of a smart anisotropic biological material. *Acta Biomater* **3**, 301–309.

ROUSSEAU, M., MEIBOM, A., GEZE, M., BOURRAT, X., ANGELLIER, M. & LOPEZ, E. (2009). Dynamics of sheet nacre formation in bivalves. *J Struct Biol* **165**, 190–195.

RYHÄNEN, R. (1962). Beobachtungrn über Häutungsvorgang und Ca-Haushalt beim Edelkrebs *Astacus astacus. Arch Soc Vanamo* **17**, 25–38.

SARDA, F. (1991). Reproduction and moult synchronism in *Nephrops norvegicus* (L.) (Decapoda, Nephropidae) in the western mediterranean is spawning annual or biennial? *Crustaceana* **60**, 186–199.

SATO, A., NAGASAKA, S., FUHIRATA, K., NAGATA, S., ARAI, S., SARUWATARI, K., KOGURE, T., SAKUDA, S. & NAGASAWA, H. (2011). Glycolytic intermediates induce amorphous calcium carbonate formation in crustaceans. *Nat Chem Biol* **7**, 197–199.

SAUER, G.R., ZUNIC, W.B., DURIG, J.R. & WUTHIER, R.E. (1994). Fourier transform Raman spectroscopy of synthetic and biogenic calcium phosphates. *Calcif Tissue Int* **54**, 414–420.

SHECHTER, A., BERMAN, A., SINGER, A., FREIMAN, A., GRINSTEIN, M., EREZ, J., AFLALO, E.D. & SAGI, A. (2008a). Reciprocal changes in calcification of the gastrolith and cuticle during the molt cycle of the red claw crayfish *Cherax quadricarinatus. Biol Bull* **214**, 122–134.

SHECHTER, A., GLAZER, L., CHELED, S., MOR, E., WEIL, S., BERMAN, A., BENTOV, S., AFLALO, E.D., KHALAILA, I. & SAGI, A. (2008b). A gastrolith protein serving a dual role in the formation of an amorphous mineral containing extracellular matrix. *Proc Natl Acad Sci USA* **105**, 7129–7134.

Soejoko, D.S. & Tjia, M.O. (2003). Infrared spectroscopy and X ray diffraction study on the morphological variations of carbonate and phosphate compounds in giant prawn (*Macrobrachium rosenbergii*) skeletons during its moulting period. *J Mater Sci* **38**, 2087–2093.

Sparkes, S. & Greenaway, P. (1984). The haemolymph as a storage site for cuticular ions during premoult in the freshwater/land crab *Holthuisana transversa*. *J Exp Biol* **113**, 43–54.

Testeniere, O., Hecker, A., Le Gurun, S., Quennedey, B., Graf, F. & Luquet, G. (2012). Characterization and spatiotemporal expression of *orchestin*, a gene encoding an ecdysone-inducible protein from a crustacean organic matrix. *Biochem J* **361**, 327–335.

Thormann, E., Mizuno, H., Jansson, K., Hedin, N., Fernandez, M.S., Arias, J.L., Rutland, M.W., Pai, R.K. & Bergström, L. (2012). Embedded proteins and sacrificial bonds provide the strong adhesive properties of gastroliths. *Nanoscale* **4**, 3910–3916.

Travis, D.F. (1955). The molting cycle of the spiny lobster, *Panulirus argus* latreille. II. Pre-ecdysial histological and histochemical changes in the hepatopancreas and integumental tisues. *Biol Bull* **108**, 88–112.

Travis, D.F. (1960). The deposition of the skeletal structures in the Crustacea. I. The histology of the gastrolith skeletal tissue complex and the gastrolith in the crayfish, *Orconectes* (*Cambarus*) *virilis* Hagen—Decapoda. *Biol Bull* **118**, 137–149.

Travis, D.F. (1963). Structural features of mineralization from tissue to macromolecular levels of organization in the decapod Crustacea. *Ann N Y Acad Sci* **109**, 177–245.

Tsutsui, N., Ishii, K., Takagi, Y., Watanabe, T. & Nagasawa, H. (1999). Cloning and expression of a cDNA encoding an insoluble matrix protein in the gastroliths of a crayfish, *Procambarus clarkii*. *Zoolog Sci* **16**, 619–628.

Urmos, J., Sharma, S.K. & Mackenzie, F.T. (1991). Characterization of some biogenic carbonates with Raman spectroscopy. *Am Mineral* **76**, 641–646.

Wehrmeister, U., Jacob, D.E., Soldati, A.L., Loges, N., Häger, T. & Hofmeister, W. (2010). Amorphous, nanocrystalline and crystalline calcium carbonates in biological materials. *J Raman Spectrosc* **42**, 926–935.

Wheeler, A.P., George, J.W. & Evans, C.A. (1981). Control of calcium carbonate nucleation and crystal growth by soluble matrix of oyster shell. *Science* **212**, 1397–1398.

Zhang, F., Cai, W., Zhu, J., Sun, Z. & Zhang, J. (2011). *In situ* Raman spectral mapping study on the microscale fibers in blue coral (*Heliopora coerulea*) skeletons. *Anal Chem* **83**, 7870–7875.

Ziegler, A. (2003). Variation of calcium deposition in terrestrial isopods. In *The Biology of Terrestrial Isopods*, vol. 2 Sfenthourakis, S., de Araujo, P.B., Hornung, E., Schmalfuss, H., Taiti, S. & Szlavecz, K. (Eds.), pp. 299–309. Leiden: Koninklijke Brill NV.

Ziegler, A., Fabritius, H. & Hagedorn, M. (2005). Microscopical and functional aspects of calcium-transport and deposition in terrestrial isopods. *Micron* **36**, 137–153.

Ziegler, A. & Miller, B. (1997). Ultrastructure of $CaCO_3$ deposits of terrestrial isopods (Crustacea, Oniscidea). *Zoomorphol* **117**, 181–187.